Ekman Transport as the Driver of Extreme Interannual Formation Rates of Eighteen Degree Water

Ke Li, Guillaume Maze, Herlé Mercier

JGR Oceans

Correspondence to:

K. Li,
ke.li@ifremer.fr

Ekman Transport as the Driver of Extreme Interannual Formation Rates of Eighteen Degree Water

Ke Li[1] , Guillaume Maze[2] , and Herlé Mercier[3]

[1]Laboratoire d'Océanographie Physique et Spatiale (LOPS), IFREMER, University of Brest, Brest, France, [2]Laboratoire d'Océanographie Physique et Spatiale (LOPS), IFREMER, University of Brest, CNRS, IRD, Brest, France, [3]Laboratoire de Physique des Océans, CNRS, UMR 6523 CNRS/Ifremer/IRD/UBO, Ifremer Centre de Brest, Plouzané, France

Abstract In the North Atlantic subtropical gyre, the Eighteen Degree Water (EDW) is a voluminous heat reservoir, submerged under a seasonal pycnocline that can be progressively removed through the winter, allowing EDW ventilation in the early spring. We target the EDW formation extremes, namely 2004–2005, 2009–2010, and 2012–2013 for the strong years, and 2007–2008, 2008–2009, 2011–2012, and 2013–2014 for the weak years. We employ gridded hydrographic datasets mainly measured by Argo floats over the last 20 years, and provide a synthetic study on the extreme events of strong and weak EDW formation of this time period. We found that the Ekman transport is the indicator and driving mechanism explaining these extremes. Strong (Weak) EDW formation years correspond with atmospheric patterns resembling NAO− (NAO+), attributed to a strong (weak) winter air-sea surface heat loss, and a strong (weak) winter heat loss due to Ekman transport. Further, we show that such extreme Ekman advection patterns can be linked to mid-latitude storms, of which both intensity and duration have an impact on the extreme of EDW ventilation in the western subtropical North Atlantic. To yield a strong EDW formation, it requires a large winter heat deficit due to Ekman divergence, which can be sufficiently represented by numbers of strong winter storms, most notably, remnants of hurricanes and US east coast snowstorms. Meanwhile, to yield a weak EDW formation, apart from weak atmospheric forcings, a remnant positive heat content anomaly carried through from previous years would serve as an unfavorable preconditioning, hindering the EDW formation.

Plain Language Summary The EDW is the most voluminous water body in the North Atlantic subtropical region. It is critical in the biology cycle and the ocean dynamics. For most of the year, EDW is buried underneath the sea surface. In winter, when sea surface loses enough heat, sinking cold water reaches the EDW bulk, forming fresh EDW. In this research, we target the EDW formation extremes, namely 2004–2005, 2009–2010, and 2012–2013 for the strong years, and 2007–2008, 2008–2009, 2011–2012, and 2013–2014 for the weak years. Using modern observational datasets, we found that the remnant hurricanes and US east coast snowstorms have an impact on the extreme interannual formation rate of EDW. To have a strong EDW formation, it is sufficient to have several strong winter storms passing by the EDW formation region, where the ocean loses more heat to the atmosphere than average over the winter. These winter-long sustained forcings have a cumulative effect on the ocean, and promote strong EDW formation. Conversely, when fewer winter storms pass, the ocean loses less heat to the atmosphere, promoting weak EDW formation. Meanwhile, the extra heat carried through from the previous years can also result in a weak EDW formation.

1. Introduction

The EDW is a nearly homogeneous water body found in the western subtropical North Atlantic region. That was named after the fact that it maintains a nearly constant temperature around 18°C. The EDW is primarily formed to the west of 45°W, between the Gulf Stream and 30°N (Maze et al., 2009). In this region, the air-sea heat flux in EDW is the key driving mechanism of EDW formation and destruction in the seasonal time scale (Forget et al., 2011; Maze et al., 2009). Maze et al. (2009) showed that in a typical seasonal cycle, intense winter surface buoyancy loss leads to the outcropping of EDW, which is replenished during this period. In the spring and summer, surface buoyancy flux destroys the EDW. Over the 2004–2006 period, Forget et al. (2011) examined the EDW volume and reported that the EDW volume increase peaked at 8.6 Svy (Sverdrup year, 1 Svy = 3.154×10^{13} m³) in February, with a total EDW volume increase due to air-sea heat fluxes of 9.3 Svy. The EDW destruction due to air-sea heat fluxes was −4.6 Svy, and that due to mixing was −2.6 Svy. The net annual

mean EDW formation due to air-sea heat fluxes and mixing was 2.0 Svy, which balanced the annual increase of EDW, about 1.4 Svy, and the annual export of EDW, about 0.6 Svy.

In addition to winter EDW renewal, subduction (Marshall et al., 1993; Qiu & Huang, 1995; R. Williams, 2001; R. G. Williams et al., 1995) and obduction (Qiu & Huang, 1995) are key processes acting on the EDW total volume. Maze et al. (2013) showed that the EDW subduction dominated by the lateral induction occurs at the southern edge of the EDW bulk area. Preconditioning is also important for the mode water formation, as it connects to the remnant mode water formed from the previous years (Piron et al., 2017; Zunino et al., 2020). To quantify the preconditioning of EDW, Billheimer and Talley (2013) investigated the buoyancy content of the water column above the permanent pycnocline in September. They found that the preconditioning impacts the EDW formation unsystematically. They also examined the horizontal Ekman advection, which is a buoyancy sink in the subtropical North Atlantic region, and is associated with southward advection of cold subpolar surface water (Billheimer & Talley, 2013; Thomas, 2005; Thomas et al., 2013). However, in the study of Billheimer and Talley (2013) and Dong and Kelly (2004), the horizontal Ekman advection is within the error bar, thus it is considered negligible on interannual time scales.

In general, the EDW bulk volume experienced a decrease since 2010 (Stevens et al., 2020). The EDW formation extreme years are documented as the following: the strong EDW formation winters are 2004–2005, 2009–2010, and the weak EDW formation winters are 2007–2008, 2011–2012, 2013–2014, and 2014–2015 (Billheimer & Talley, 2013, 2016). Billheimer and Talley (2013); Billheimer and Talley (2016) addressed that a strong (weak) EDW formation extreme is correlated with a strong negative (positive) wintertime North Atlantic Oscillation (NAO). Peng et al. (2006) used modeling indicating a lagged correlation between NAO and EDW annual subduction rate at Panulirus station (32°10′N, 64°30′W) near Bermuda. They found that the lag is 2–3 years with NAO leading.

We aim to better understand how the EDW evolved over the past 20 years by looking into the EDW formation extremes and the dynamics behind these events. The modern observational datasets feature high precision and resolution, particularly in the subtropical North Atlantic region, which enables a systematic study on EDW extreme events. A presentation of our methodology is given in Section 2. EDW formation extreme are identified in Section 3.1. Thereupon, we aim to decipher the mechanisms behind the occurrences of extreme years. The atmospheric patterns corresponding to the strong and the weak EDW formation events are investigated in Section 3.2 and 3.3. This includes verifying the role of air-sea surface heat fluxes in EDW extreme events. We estimated the Ekman heat transport in the western subtropical North Atlantic region and unveiled the pre-eminent role of the Ekman heat convergence/divergence in EDW formation extremes. We further investigated the Ekman heat transport from the perspective of the weather events, by addressing the following question: Are the extreme EDW formations due to several strong weather events or to some constant signals over wintertime? Lastly, we addressed the preconditioning in subtropical North Atlantic region, with regard to the EDW formation (Section 3.4 and 3.5). We conclude in Section 4.

2. Methodology

2.1. Domain of Study

The EDW ventilation takes place in the early spring in the EDW formation region or the EDW outcropping area delimited by the two red solid lines in Figure 1. We chose the domain of analysis (the black dashed lines in Figure 1) to include the EDW formation region. The northern boundary of the domain of study is at the northern flank of the Gulf Stream (38°N, 75°W–46°N, 35°W), to ensure the inclusion of the mode water outcropping area. The southern boundary is 30°N, and the eastern boundary is located at 35°W, east of the standing Mann Eddy at the Gulf Stream extension (45°W, 42°N). Surrounding the Mann Eddy, the Gulf Stream turns northward to exit the domain of study from the northern boundary and becomes part of the North Atlantic Current (NAC). The western boundary is located at 75°W at the entrance of the Gulf Stream, with a reasonable distance from the coastal region.

The vertical domain, which extends from the sea surface to 800 m in depth, contains the EDW bulk. Eight hundred meters is below the maximum depth that EDW can reach in the domain of analysis, at both the outcropping and the subduction region, and was tested true for all the employed datasets. The total surface area of the domain
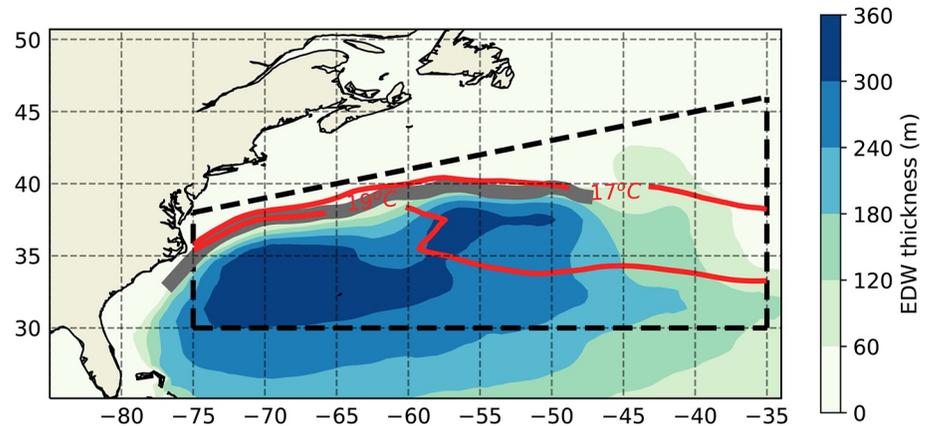
Figure 1. The domain of study (the black dashed line) and the climatological mean of EDW thickness (color shading in blue) for 2003–2018. The thick solid gray line shows the SSH (sum of the sea level anomaly, SLA, and mean dynamic topography, MDT, from AVISO Altimetry) at 0.39 m, indicating the Gulf Stream position. The red solid contours indicate the 17°C and 19°C early spring outcropping mean position over the period of 2003–2018. The EDW thickness is calculated using the potential density layer of 26.2–26.6 kg m^{-3}, and the PV threshold of PV $< 1.5 \times 10^{-10}$m^{-1}s^{-1}. The PV is calculated using the potential density and the Brunt-Väisälä frequency from ISAS15-ARGO data.

of analysis is 4.918×10^{12} m^2, and the total volume of seawater in the domain of analysis is 3.93×10^{15} m^3 (127.7 Svy).

2.2. Data Sets

Regarding the ocean, we used ocean datasets that are based on an optimal interpolation of in-situ data. We used ISAS15-ARGO monthly analysis for the period of 2002–2015 and ISAS-NRTOAGL01 monthly analysis for January 2016–April 2020 (Table 1, altogether referred to as the ISAS dataset; Kolodziejczyk et al., 2017), taking the practical salinity and the temperature. The data source of ISAS15-ARGO and ISAS-NRTOAGL01 are Argo only. These are gridded datasets with a meridional resolution of 0.5° in latitude and a zonal resolution varying from 0.45° at a latitude of 25°N–0.32° at a latitude of 51°N. The maximum depth level is 2000°m. We used the monthly EN4 dataset for the period of January 2002–March 2020 (Table 1; Good et al., 2013), taking the in-situ temperature and the salinity. The data source of EN4 consists of Argo, ASBO (Arctic Synoptic Basin Wide Oceanography), GTSPP (Global Temperature and Salinity Profile Program), and World Ocean Database

Table 1
List of the Datasets Employed in the Analysis

Dataset	Temporal Coverage	Resolutions	Reference
	Ocean Datasets: Temperature and Salinity		
EN4	January 1950–March 2020	1.0°, monthly	Good et al. (2013)
ISAS	January 2002–April 2020	0.5°, monthly	Kolodziejczyk et al. (2017)
Scripps	January 2004–January 2020	1°, monthly	Roemmich and Gilson (2009)
IPRC	January 2005–December 2019	1°, monthly	APDRC (2009)
	Altimetry Datasets: SSH		
SSH anomaly	January 1993–May 2019	0.25°, monthly	CMEMS (2020)
MDT	1993–2012 mean	0.25°, climatology	Rio (2009)
	Atmosphere Datasets		
	Sea level pressure, Geopotential height at 500 hPa,		
	Air-sea heat fluxes, Surface wind speed, Surface wind stress momentum flux		
NCEP	January 1948–Febuary 2020	2.5°, 6 hr	Kalnay et al. (1996)
ERA	January 1979–January 2020	0.75°, daily	Dee et al. (2011)

(WOD). The EN4 dataset has a horizontal resolution of $1° \times 1°$ and a maximum depth level of 5,350 m. We also used Roemmich-Gilson dataset from the Scripps Institute of Oceanography (the Scripps dataset), a Global gridded 1 degree Argo only dataset (Table 1; Roemmich & Gilson, 2009). The Scripps dataset covers the period of January 2004-January 2020. The maximum depth level of the Scripps dataset is 1,953.01 m. The International Pacific Research Center (IPRC) monthly dataset (the IPRC dataset) is based on Argo temperature and salinity, and has a horizontal resolution of $1° \times 1°$. The IPRC dataset covers the period of January 2005-December 2019. The maximum depth level of the IPRC dataset is 2,000 m. We used the Gibbs Seawater Library (GSW) version 3.0.3 to calculate the seawater in-situ density and the potential vorticity (PV). To estimate horizontal velocities, we used the altimetry datasets that include the sea surface height (SSH) anomaly, which cover the period of January 1993-May 2019, and the SSH mean or Mean Dynamic Topography (MDT). The SSH anomaly comes from the global ocean gridded L4 SSHs and derived variables reprocessed (1993-ongoing; Product ID: SEA-LEVEL_GLO_PHY_L4_REP_OBSERVATIONS_008_047) distributed by the Copernicus Marine Environment Monitoring Service (CMEMS, 2020). The SSH mean comes from the CNES-CLS2013 Mean Dynamic Topography (MDT; Rio, 2009). The altimetry datasets have a horizontal resolution of $0.25° \times 0.2°$.

Regarding the atmosphere, we used the sea level pressure (SLP), the geopotential height at 500 hPa, the air-sea surface heat fluxes, the surface wind speed, as well as the surface wind stress momentum flux from National Centers for Environmental Prediction-National Center for Atmospheric Research (NCEP-NCAR, or NCEP) reanalysis data (Kalnay et al., 1996). We used the NCEP dataset in the period of 2002–2019 with a 6-hr time resolution and $2.5° \times 2.5°$ horizontal resolution. In addition, we used European Center for Medium-Range Weather Forecasts (ECMRWF) Reanalysis data (ERA-interim, or ERA5, Dee et al., 2011). We used the ERA dataset in the period of January 2002–January 2020 with a daily time resolution and $0.75° \times 0.75°$ horizontal resolution.

2.3. Mixed Layer Depth (MLD) and Ventilated EDW Volume

The density-mixed layer depth (DMLD) is the depth of upper ocean where potential density becomes larger than the 10-m value by a fixed $\Delta\sigma_0$. We employed the density threshold of $\Delta\sigma = 0.03$ kg m^{-3} to estimate the mixed layer depth of the ISAS, EN4, IPRC and Scripps datasets (de Boyer Montégut et al., 2004).

We computed the EDW ventilated volume, not including the EDW that is trapped under the mixed layer. We selected the surface EDW outcropping regions, with sea surface potential density ranging from 26.2–26.6 kg m^{-3}, integrated this outcrop down to the MLD, and selected the seasonal maximum of the EDW ventilated volume within a year. From here on, unless specially specified, the EDW ventilated volume refers to the seasonal maximum.

We aimed to capture the interannual variability of this EDW ventilated volume. We applied a high-pass filter of 10 years to remove the multidecadal signal. We defined the EDW ventilated volume extreme as the outliers that exceeds ± 1.0 the standard deviation of the interannual variability of EDW ventilated volume.

2.4. Buoyancy Content Anomaly

The buoyancy anomaly of a water parcel is defined as:

$$b = \frac{g}{\rho_\circ}(\sigma - \sigma_\circ) \tag{1}$$

where, b is the buoyancy anomaly in the unit of m s^{-2}, g is gravity, $(\sigma - \sigma_\circ)$ is the relative density difference between a water parcel and that at the bottom of EDW (the upper part of the permanent pycnocline), where $\sigma_\circ = 26.7$ kg m^{-3} (Feucher et al., 2019).

We define the buoyancy content anomaly (BCA), as the integration of buoyancy anomaly b in Equation 1 from the March mixed layer depth MLD$_{Mar}$ (the deepest mixed layer depth in an EDW formation season) to the surface, as well as over the surface area (S) of the domain of analysis:

$$BCA = \int_S \int_{MLD_{Mar}}^{z=0} b\, dz\, dS \tag{2}$$

where the unit of the BCA is m^4 s^{-2}. Accordingly, the preconditioning at the beginning of the winter EDW ventilation period is described by BCA$_{Sep}$, with an integration over the following March mixed layer each year. Note that the March mixed layer depth varies on an interannual basis. The buoyancy in September (BCA$_{Sep}$) of each year largely depends on the upper ocean volume associated with this March MLD. Accordingly, we rescaled BCA$_{Sep}$ by the coming March mixed layer depth in order to evaluate the preconditioning. Thus we define the preconditioning term BCA$^*_{Sep}$ using:

$$BCA^*_{Sep} = \frac{1}{S} \cdot (BCA_{Sep}/MLD_{Mar}) \tag{3}$$

where BCA$^*_{Sep}$ is the scaled buoyancy content anomaly, which for convenience will be reported in the heat content unit of (J m^{-3}). MLD$_{Mar}$ refers to March of the current year, and BCA$_{Sep}$ refers to the September of the previous year, in the unit of m^4 s^{-2}. $S = 4.918 \times 10^{12}$ m^2 denotes the horizontal surface of the domain of analysis.

Note that the wintertime of a year refers to the period from September of the previous year to March of the current year. For example, September 2009-March 2010 is denoted as the winter of 2010 (Winter10).

2.5. Heat Advection Due to Ekman Transport

The heat source due to the convergence of the Ekman heat transport $\mathcal{H}_{Ek}$ is:

$$\mathcal{H}_{Ek} = -\rho_\circ C_p \nabla_{\mathbf{H}} \cdot (\mathbf{U}_{Ek}\ SST) \tag{4}$$

where $\rho_\circ = 1.027 \times 10^3$ kg m^{-3} is the reference ocean density, and $C_p = 4.2 \times 10^3$ J kg^{-1} °C^{-1} is the sea water specific heat. $\boldsymbol{U}_{Ek}$ denotes the Ekman transport.

The transient ocean response to the storms vanishes after a few days when the ocean response can be well approximated by the steady Ekman transport (Vincent et al., 2012, 2013). Therefore, we considered the ocean response to the storms as the steady Ekman heat transport that was, in this paper, estimated with a monthly time resolution.

Note that $\mathcal{H}_{Ek}$ and the air-sea surface heat flux (integrated over the surface area S) Q_{net} are forcings, in the unit of W. We calculated the interannual time series of these two terms first. Meanwhile, we aim to understand the heat content change of the EDW formation region ascribable to the Ekman heat flux and the air-sea surface heat flux. Thus, we integrated both time series over time from 2002 to obtain the accumulated Ekman heat flux and the accumulated air-sea surface heat flux, in ZJ (zettajoule, 1 ZJ = 1×10^{21} J). For the naming convention purpose, the Ekman heat convergence (divergence) refers to a positive (negative) anomaly of the accumulated Ekman heat flux. A negative (positive) anomaly of the accumulated air-sea surface heat flux signifies a stronger (weaker) air-sea surface heat loss than its typical seasonal cycle.

3. Direct Results

3.1. EDW Ventilated Volume Extremes

We focus on the Argo era (after 2000) to examine the interannual variability of EDW ventilated volume and the extreme EDW formation years from different Argo observational reanalysis products (Figure 2). We chose as the extreme years of EDW formation the years with the mean value exceeding the standard deviation $\sigma = 2.86$ Svy. The years 2005, 2010 and 2013 are extreme years of strong EDW ventilation, while 2008, 2009, 2012, and 2014 are extreme years of weak EDW ventilation.

3.1.1. Extreme Years of EDW Formation

Here, we used the area between 17–19°C isotherms to track the interannual variability of the EDW surface outcropping region when it reaches its annual maximum in March (the blue solid curves in Figure 3). In the strong years, the outcropping area is larger than that in weak years (Figures 3a–3c). EDW being renewed, the EDW surface outcropping region reaches seasonal maximum in March. The mixed layer depth is deep in the strong years (the black solid curves in Figure 3), 250 m in 2005, 350 m in 2010, and 2280 m in 2013, testifying of deep convection. In the weak years, the outcropping area is small compared with that of the strong years (Figures 3d–3g), as the EDW surface outcropping region does not open up as much as in the strong years. The March mixed layer depth is less than 100 m in the weak years, shallow compared to the strong years. As the result, the
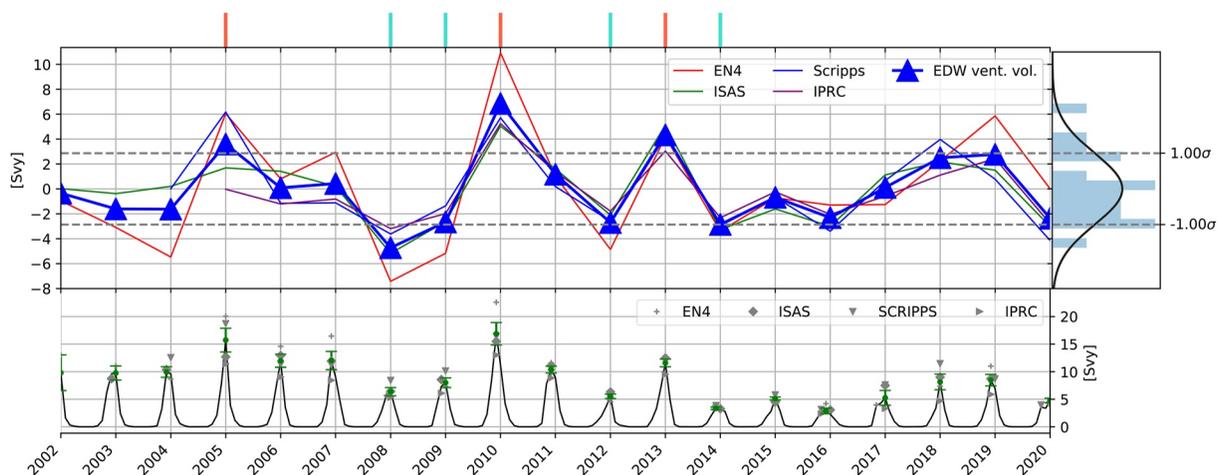
Figure 2. (Upper) 2002–2020 interannual variability of EDW ventilated volume, in units of Svy (the blue curve). In thin green line is the EDW volume calculated using the ISAS dataset, EN4 in red, Scripps in blue, and IPRC in purple. The gray dashed lines are the standard deviations ($\sigma = 2.86$ Svy) of the interannual EDW ventilated volume time series. The histogram of interannual EDW formation volume values is represented to the right, superimposed with a Gaussian fit (solid black curve). The selected extreme years are indicated in the "rug" plot. In short solid red lines are the strong years. In cyan are the weak years (Lower) The monthly time series of the EDW ventilated volume (solid black line), with dots indicating the seasonal maximum. The green error bars indicate the unbiased standard deviations among four data products (EN4, ISAS, Scripps, and IPRC) at the seasonal maximum.

EDW ventilation is weak, which further can lead to a near cessation of EDW formation, as in 2012 when the poorly stratified water at the surface was not able to penetrate down to the EDW bulk (the light purple shades in Figure 3d). These two poorly stratified water bodies are separated by a layer of stratified water in the middle. The EDW ventilation in the early spring of 2012 experienced a near cessation.
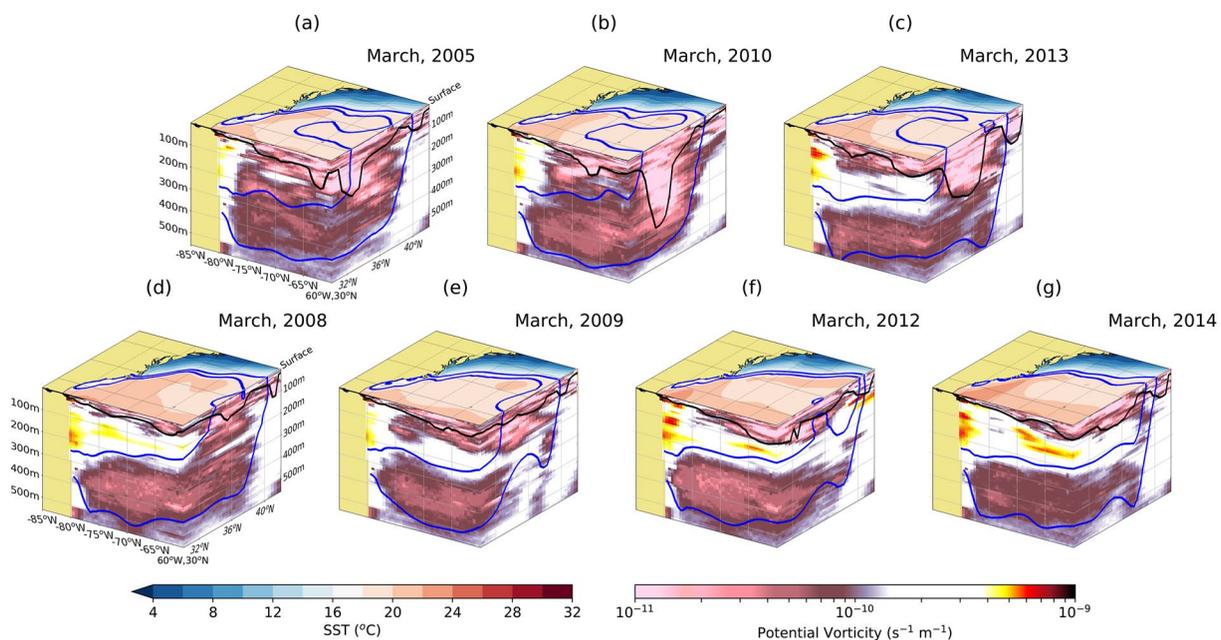

Figure 3. The early spring EDW ventilation during the EDW extreme years. The top row: (a–c) are the strong years, namely, 2005, 2010, and 2013. The bottom row: (d–g) are the weak years, namely, 2008, 2009, 2012, and 2014. The color shades at two side cross-sections denote the potential vorticity in m^{-1} s^{-1}. Dark red is the stratified water, and light purple is homogeneous water. Between the blue curves is the averaged 17–19°C EDW outcropping region. The black line is the deepest mixed layer depth. At the surface, the color shades denote the SST in °C. This plot was realized using the ISAS dataset.
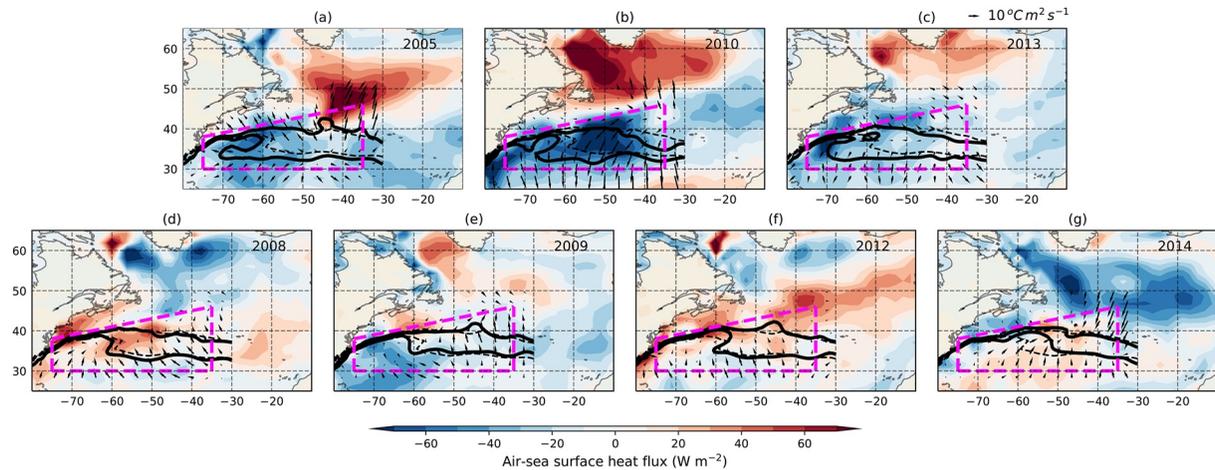
Figure 4. The surface EDW outcropping region, the wintertime air-sea surface heat flux anomalies, the Ekman temperature transport of extreme years of strong EDW formation: (a) 2005, (b) 2010, and (c) 2013, as well as of weak EDW formation: (d) 2008, (e) 2009, (f) 2012, and (g) 2014. The color shades indicate the wintertime air-sea surface heat flux anomalies, in W m^{-2}. The black arrows indicate the Ekman temperature transport in °C m^2 s^{-1}. The black solid contours and the black dashed contours denote, respectively, the 2002–2020 interannual mean position and the yearly position of 17°C and 19°C isotherms at the ocean surface at the time of the annual deepest mixed layer. The SST is from the ISAS dataset. The surface wind stress and the air-sea surface heat flux are from the NCEP dataset.

3.2. Atmospheric States

Figure 4 shows the atmospheric state variables in March, corresponding with the annual maximum of EDW outcropping for the extreme years of EDW formation. Among the extreme strong years of EDW formation, namely, 2005, 2010, and 2013, we observed Ekman heat divergence in the domain of study, dominated either by strong northward transport from the northern boundary, as in 2005, strong southward transport at southern boundary, as in 2010 (Figure 4b), or both, as in 2013 (Figure 4c). Moreover, we observed strong air-sea surface heat flux anomalies in the domain of study (Figure 4e). The EDW surface outcropping region of the strong years are larger than average, with a notable extra extension toward the center of the North Atlantic subtropical gyre.

Among the extreme years of weak EDW formation, for example, 2008, 2009, 2012, and 2014, we observed the horizontal Ekman heat convergence in the domain of study, dominated either by strong northward transport from the southern boundary alone as in 2008 (Figure 4d), in 2009 (Figure 4e), and in 2012 (Figure 4f), or in combination with strong southward transport from the northern boundary, as in 2014 (Figure 4g). The wintertime air-sea surface heat flux in the domain of analysis is weaker than average. The EDW outcropping area can be smaller than average, as in 2014. Or the outcropping area can be shifted without changing the size compared with the 2002–2020 climatological mean, as in 2008, 2009, and 2012. However, the early spring mixed layer depth in the weak years is shallow, no more than 100 m in depth, compared with strong years (first line in Figure 3).

3.3. EDW Driving Mechanisms

3.3.1. Atmospheric Composites for Extreme EDW Formations

We investigated the atmospheric variable composites attributed to the extreme years of EDW formation (Figure 5). Among the extreme years of strong EDW formation, the negative sea level pressure is centered in the central subtropical North Atlantic region, and the positive sea level pressure is centered between Iceland and the southern tip of Greenland, above the Irminger Sea region (Figure 5a). This sea level pressure pattern resembles the NAO− (Cassou et al., 2004). For the weak EDW formation, the sea level pressure composite is almost opposite to the strong years. This composite resembles NAO+ (Cassou et al., 2004), with the centers of the low and high sea level pressure patterns shifted eastward.

Regarding the air-sea surface heat flux, we observed that in the western subtropical North Atlantic region, strong (weak) wintertime air-sea surface heat loss corresponds with strong (weak) EDW formation (Figures 5c and 5d). The exceptions are 2005 and 2009, two extreme years in EDW formation, with average air-sea surface heat flux anomalies, within ±1 σ (Figure 6a).
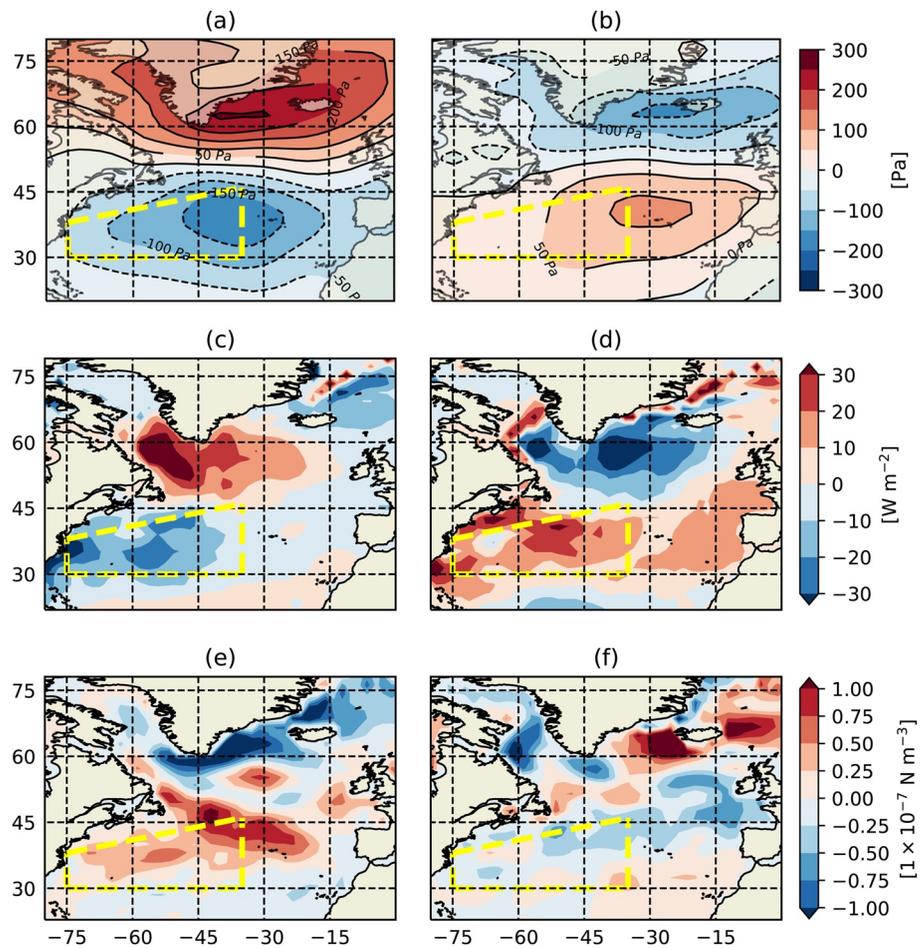
Figure 5. Composites of atmospheric variables for strong (left) and weak (right) wintertime EDW formation extremes: (a and b) sea level pressure, in the unit of Pa (c and d) air-sea heat flux, in the unit of W m^{-2}, and (e and f) surface wind stress curl, in the unit of 1×10^{-7} N m^{-3}. The composites are calculated as the September-March average of these variables for the strong and weak extreme years. We used the NCEP dataset to produce these plots.

We examined the wind stress curl composites (Figures 5e and 5f). During the strong EDW formation extreme years, we observed a positive anomaly $>0.4 \times 10^{-7}$ N m^{-3} located in the central subtropical North Atlantic region (45°N, 30° − 45°W, to the northeast of the EDW formation region. On the opposite, during the weak EDW formation extreme years, we observed a negative anomaly of the wind stress curl with a value of $< -0.1 \times 10^{-7}$ N m^{-3} (Figure 5f). The negative sign indicates weaker than normal surface wind stress curl. To link to the Ekman current, a positive (negative) anomaly of the wind stress curl in the domain of study indicates anomalous cooling (warming) due to the Ekman heat divergence (convergence).

The Ekman heat flux serves as an indicator of the extreme years of EDW formation (Figure 6b). The extreme years of weak EDW formation, namely, 2008, 2009, 2012, and 2014 correspond with the Ekman heat convergence, indicating anomalous warming in the domain of analysis. The extreme years of strong EDW formation, namely, 2005, 2010, and 2013 correspond with the Ekman heat divergence, indicating anomalous cooling in the domain of analysis.

In both strong and weak extreme formation years, the contribution of the Ekman heat flux is as large as that of the air-sea surface heat flux. For example, in 2009–2010, the accumulated Ekman heat flux is −3.5 ZJ, and the accumulated air-sea surface heat flux is −2.4 ZJ (Figure 6b). Similarly, in 2011–2012, the accumulated Ekman heat flux is 1.8 ZJ, and the accumulated air-sea surface heat flux anomaly is 1.5 ZJ.
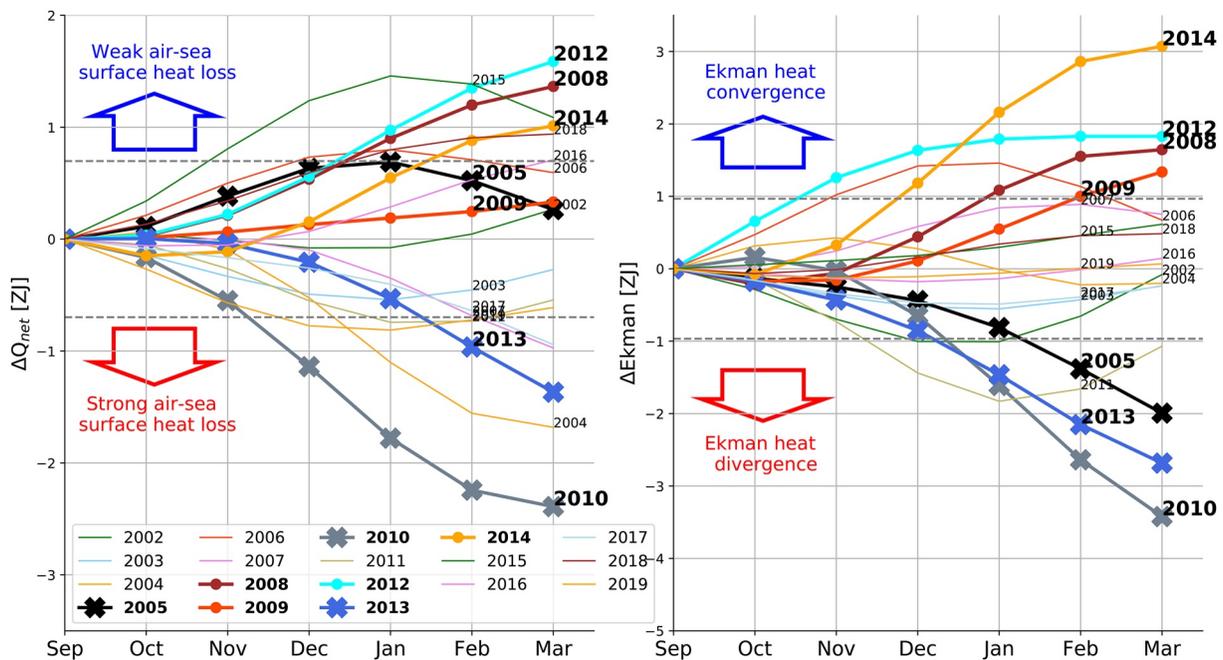
Figure 6. The 2002–2019 September-March accumulated air-sea surface heat flux (ΔQ_{net} in (a) and the accumulated Ekman heat flux (ΔEkman in (b), both in ZJ (1 ZJ = 1 × 10²¹ J). The dashed gray lines indicate 1 standard deviations from the mean ($\sigma = 0.7$ ZJ in (a), and $\sigma = 0.97$ ZJ in (b). The thick solid lines are EDW formation extreme years, with strong years in ×, and weak years in •. Both variables were calculated as the average of the ERA and the NCEP datasets.

Figure 7. The 2003–2019 September–March, daily accumulated "no-smoothing" anomalies of the heat convergence due to Ekman advection. Similar to Figure 6b, except this plot is in daily time resolution. The dashed gray lines indicate the standard deviation $\sigma = 1.24$ ZJ.

3.3.2. Effect of Storminess

We took one step further to understand the role of the Ekman heat flux from the perspective of the weather events. We investigated the daily progression of the accumulated Ekman heat flux during the EDW formation period of each year (Figure 7). We removed the typical seasonal cycle to obtain its daily anomaly compared to a typical year. For example, a decrease in the accumulated Ekman heat flux (Figure 7) indicates a cooling effect in the domain of analysis, which can be associated with low pressure systems passing by the domain of analysis.

In September and October, the passing storms are mainly subtropical cyclones and hurricanes, decaying in magnitude as they move northward, passing by the domain of analysis. We use the winter of 2013 (September 2012−March 2013) as an example. Hurricane Sandy passed the domain of study during 26–30 in October 2012 (Blake et al., 2013), responsible for a cooling by a negative accumulated Ekman heat flux of −0.9 ZJ for 9 days (the blue curve in Figure 8b). Hurricane Sandy is responsible for 23% of the total amount of cooling due to the Ekman heat flux in the wintertime of 2013.

From 20 November 2012–mid−January 2013, three storms, each occurring one month apart, brought a total Ekman-associated cooling of −1.5 ZJ, 38% of the total amount of Ekman-associated cooling in the wintertime of 2013 (Table A2 in Li, 2020). Included in these storms is the prelude to Wind Storm Gong, which brought destructive high winds to Portugal (Liberato, 2014) and the aftermath of the 2012 Mid-December Blizzard (NWS, 2015; NWS, 2016), featuring heavy snowfalls and gusty winds in the US Midwest (Figure 8c). These blizzards often enter the domain of analysis from the northern boundary. From 21 February–10 March 2013, two consecutive blizzards, namely the Late February Winter Storm and the March Nor'easter (NWS, 2019; Ryan
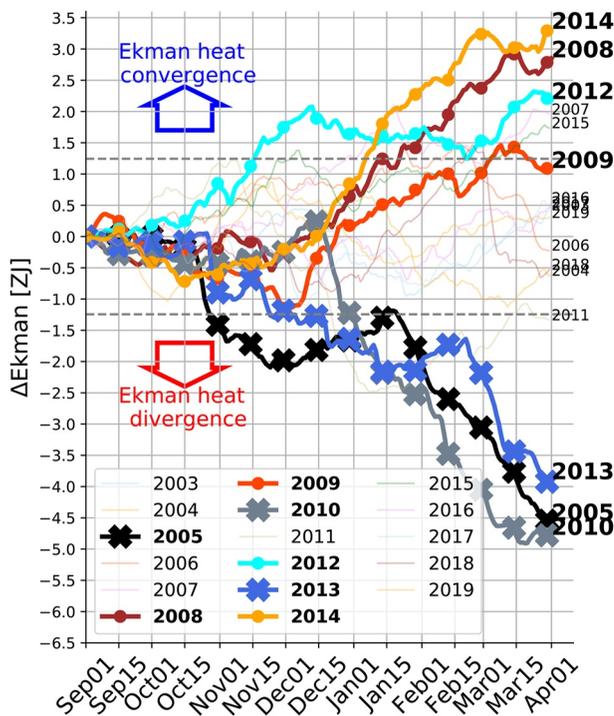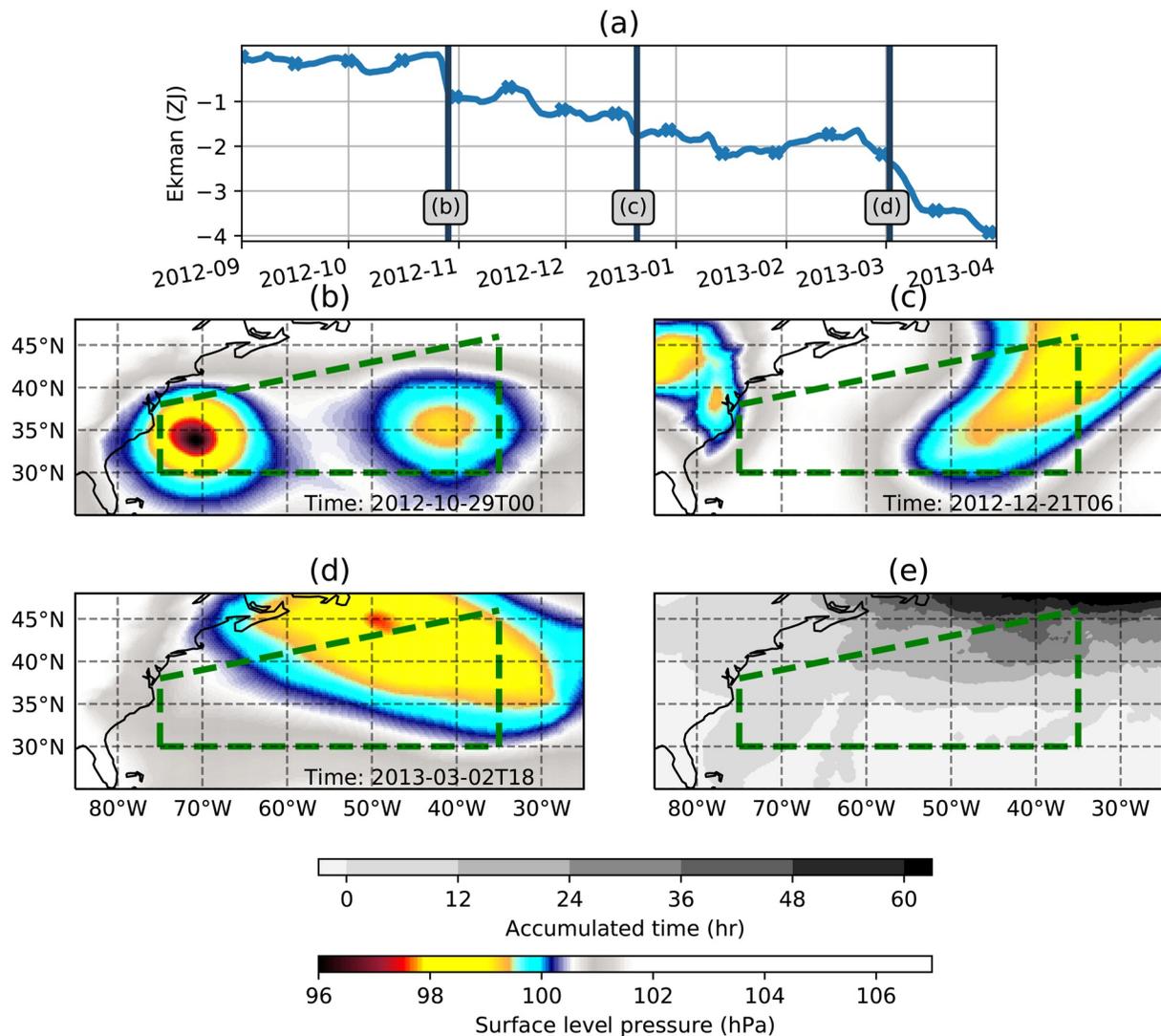
Figure 8. (a) The 2013 accumulated Ekman heat flux taken from Figure 7, in daily resolution, in ZJ. We chose three storms shown in (b) Hurricane Sandy at 00:00UTC on 2012-10-29, (c) the mid-December North America blizzard at 06:00UTC on 2012-12-21, and (d) the nor'easter blizzard at 18:00UTC on 2013-03-02. The color shades indicate the surface level pressure of the storms passing by the domain of analysis, in hPa. (e) The September-March accumulated hours of passing storms (in gray shades). The plot (a) was realized using both NCEP and ERA. The individual storms in (b–d) are plotted using ERA 6-hr surface level pressure dataset. Regarding the method used to calculate the accumulated hours, see details in Section 3.3.2.

et al., 2014), passed the domain of study (Figure 8d). The two typical blizzards during this time of year had a wide impact on US South, Midwest, and east coast states.

To estimate the storms' impact to the Ekman heat flux, we identified as storms the low pressure systems that maintain a center value of ≤990 hPa (Betts et al., 2004; Haak & Ulbrich, 1996) in the domain of analysis for, at the minimum, two consecutive days. In the winter of 2013, the total duration of storms passing by the domain of analysis is 108 days (Table 2). The spatial distribution of the local accumulated hours due to storms is centered at the northeast corner of the domain of analysis, ≥36 hr/pixel, and is ≥12 hr/pixel north of 35°N (Figure 8e). This indicates that the storms mainly passed by the northern part of the domain of analysis near the Gulf Stream, where the EDW outcropping starts in the early spring.

As the next step, we quantified the impact of the storm-induced Ekman heat flux on the EDW extreme years. We report in Table 2 the total winter storm duration, the accumulated wintertime Ekman heat flux, and the mean wintertime Ekman heat flux. Of the strong extreme EDW renewal years, the mean wintertime Ekman heat flux, and the accumulated storm duration are at higher percentile ranks (>50%) of the year 2000–2020 (Table 2). The 2005

Table 2

Table of the Impact of the Late Fall and Winter Storms During the Extreme EDW Ventilation Years

Year	Storm-associated accumulated Ekman heat flux (ZJ, negative)	Accumulated storm duration (day)	Storm-associated Ekman heat flux (W m^{-2}, negative)
× 2005	6.0 (87.5%)	133 (max)	106.7 (68.8%)
• 2008	2.4 (18.8%)	78 (25%)	70.8 (min)
• 2009	3.2 (38.9%)	82 (33.3%)	92.3 (55.6%)
× 2010	6.9 (max)	128 (93.8%)	126.9 (87.5%)
• 2012	2.7 (31.2%)	77 (18.8%)	82.3 (43.8%)
× 2013	6.5 (93.8%)	108 (87.5%)	140.7 (max)
• 2014	1.9 (min)	60 (min)	72.9 (12.5%)

Note. The storm-associated accumulated Ekman heat flux (in ZJ), storm duration (in day), and the storm-associated Ekman heat flux (W m^{-2}) during the extreme EDW ventilation years. In parentheses are the percentiles. The percentile of the correspondingly indicated value signifies the percentage of samplings whose values are less or equal to this indicated value. For example, in 2008, the accumulated storm duration is 78 days, with a percentile of 25%. That indicates that 25% of the years examined, namely 2002–2020, have the accumulated storm duration less or equal to 78 days. Marked in × are the extreme years of strong EDW formation. Marked in • are the weak years.

Figure 9. The 2002–2019 BCA$^*_{Sep}$ in J m^{-3}. Horizontal axis indicates the EDW ventilated volume in Svy. The strong EDW formation years are marked in red, and the weak years in blue. Toward the top of the vertical axis are the years with a less favorable preconditioning to the EDW formation, and toward the bottom a more favorable preconditioning. Toward the top, the surface water is lighter and more buoyant than the years toward the bottom.

period has the longest storm duration. The 2010 period has the largest negative anomaly of the total storm-associated accumulated Ekman heat flux, while the 2013 period has the largest storm-associated Ekman heat flux. The total wintertime Ekman-associated cooling due to storms is sufficient to separate the extreme years of strong EDW formation from the remaining years.

In 2014, a weak extreme EDW formation year, the total amount of the storm-associated accumulated Ekman heat flux is −1.9 ZJ (Table 2), and the accumulated storm duration is 60 days. Both of these values are minima in the 2000–2020 period. In 2008, another weak extreme EDW renewal year, the Ekman heat flux averaged over the wintertime is −70.8 W m^{-2}, the smallest heat flux anomaly due to Ekman transport in the 2000–2020 period. In 2009 and 2012, the accumulated storm duration has percentiles of 33.3% and 18.8% respectively, and the total amount of Ekman-associated cooling due to storms has percentiles of 38.9% and 31.2% respectively.

In short, in the strong EDW formation years, namely, 2005, 2010, and 2013, we observed the remnant storms from decaying hurricanes in the late fall, and the blizzards in winter and early spring. These storms move off the US east coast, and pass by the domain of study. Of these strong years, these storms during the EDW formation period are responsible for the sudden decrease in the accumulated heat flux due to Ekman current (Figure 7). In the weak EDW formation years, namely, 2008, 2009, 2012, and 2014, we observed fewer and weaker winter storms, which result in shorter total storm duration and weaker Ekman-associated cooling due to storms than those of the strong years.
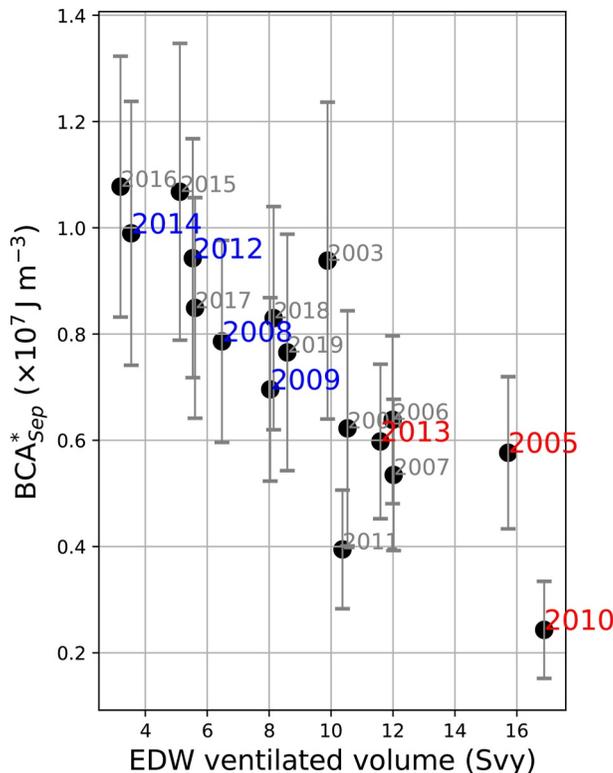
3.4. Preconditioning

BCA$^*_{Sep}$ describes the vertical distribution of the buoyancy content in September that potentially turns into a deep convection in the early spring. A smaller (larger) BCA$^*_{Sep}$ indicates a less (more) buoyant September upper water column, a favorable (an unfavorable) preconditioning to a deep convection in the coming early spring (Figure 9).

The BCA$^*_{Sep}$ distinguishes the strong and weak EDW formation years (marked in red and blue in Figure 9, respectively). Of the strong years, BCA$^*_{Sep}$ of 2010 is 0.25 × 10^7 J m^{-3}, the smallest among all. Its unbiased standard error is ±0.1 × 10^7 J m^{-3}, indicating a robust favorable preconditioning. BCA$^*_{Sep}$ of 2015 and that of 2016 are the largest (1.07 ± 0.2) × 10^7 J m^{-3}, unfavorable to the deep convection in the coming early spring. Note that among the weak years, 2008 and 2009 have average values of BCA$^*_{Sep}$ of 0.79 × 10^7 J m^{-3} and 0.7 × 10^7 J m^{-3} (Figure 9). This indicates that the preconditioning of 2008 and 2009 neither promotes nor hinders an early spring deep convection, compared with other years. The preconditioning is not the lead driving factor to the weak early-spring EDW formation of these 2 years.

3.5. A Brief Summary of the Direct Results

We have examined the impact of the Ekman heat flux, the air-sea surface heat flux, and the preconditioning on the EDW ventilated volume in the early spring. We synthesized these factors into Table 3 to investigate their respective contributions to the extreme years of EDW early spring formation (the column "EDW volume" in Table 3). For each year, we attributed a score to the contribution of each factor, which was calculated as the original value

Table 3
2003–2019 Newly Formed EDW Volume, Wintertime Forcing, and Preconditioning Score Table

Year	Accumulated Ekman heat flux	Accumulated Air-sea heat flux	Pre-conditioning	Total	EDW volume	NAO−	NAO+
2003	0.4	−0.8	0.9	−0.5	−0.6	0.6	−1.8
2004	−0.5	−2.3	−0.5	−4.0	−0.6	−0.3	−0.7
× 2005	−3.6	−0.7	−0.8	−5.1	1.3	0.1	−0.8
2006	−0.1	0.3	−0.5	−0.6	0.0	0.5	−1.2
2007	1.6	−0.6	−0.9	−0.4	0.2	0.2	1.3
● 2008	2.3	1.9	0.2	4.4	−1.6	−1.2	0.9
● 2009	0.9	−0.1	−0.2	1.0	−0.9	−0.5	0.2
× 2010	−3.8	−3.4	−2.3	−9.2	2.4	2.2	−0.8
2011	−1.0	−0.7	−1.6	−3.9	0.4	1.3	−0.8
● 2012	1.8	1.9	0.9	4.3	−0.9	−1.5	1.1
× 2013	−3.1	−1.2	−0.7	−4.8	1.5	1.9	−0.8
● 2014	2.7	1.8	1.1	5.5	−1.0	−0.5	2.0
2015	1.4	1.6	1.5	5.1	−0.2	−0.8	0.9
2016	0.5	1.3	1.5	4.2	−0.8	−0.3	0.9
2017	0.4	−1.6	0.5	1.4	0.0	−0.8	−0.8
2018	−0.4	0.5	0.4	1.1	0.9	−0.1	−0.3
2019	0.3	−1.3	0.1	0.4	1.0	−0.9	0.1

Note. The score is calculated as the original value subtracted by the mean and then divided by the standard deviation. In each column, the table content is in times of standard deviation of the corresponding time series. The preconditioning refers to the BCA^*_{Sep}. We listed as the wintertime forcing the accumulated Ekman heat flux, and the accumulated air-sea surface heat flux. Of each year, we calculated "Total" as the sum of the scores of the preconditioning and those of the wintertime forcings. The wintertime is defined as the period of September of the previous year to March of the current year. ● indicates the extreme years of weak EDW formation. × indicates the extreme years of strong EDW formation. In the NAO− (+) column, the table content is the score of wintertime "NAO− (+)" occurrence (Cassou et al., 2004), calculated as the average of the ERA and the NCEP datasets, using 500 hPa geopotential height and surface level pressure.

subtracted by the mean and then divided by the standard deviation. We summed the scores of all factors to yield the total score (the column "Total" in Table 3).

The year 2005 is an extreme year of strong EDW formation, of which the main driver is the strong Ekman heat divergence. Its score for the Ekman term is −3.6 standard deviation (Table 3), where the negative sign indicates divergence. This Ekman score is one of the largest negative values in the period of 2003–2019, second after 2010. The other factors, such as the accumulated air-sea surface heat flux, and BCA^*_{Sep} are comparably weak. Yet, in total, the forcings of 2005 are strong compared with other years, with a total score of −5.1. The negative sign indicates the cooling associated with the strong forcings. Therefore, the 2005 EDW ventilated volume is on the higher end of the spectrum than other years, with a score of 1.3.

The year 2010 is an extreme year of strong EDW formation. The contributing factors include the large negative Ekman heat flux, with a score of −3.8 (Table 3), the large negative air-sea surface heat flux, with a score of −3.4, and the favorable preconditioning of BCA^*_{Sep}, with a score of −2.3. The total score is −9.2, which indicates strong forcings with a favorable preconditioning. The 2010 EDW ventilated volume has a score of 2.4 of its standard deviation, the strongest among all years, indicating an exceptional EDW formation in 2010.

More generally, among the extreme years of strong EDW formation (marked in "×" in Table 3), the EDW ventilated volume is positive, and the total score is negative. The accumulated Ekman heat flux of 2005, 2010, and 2013 is negative with large amplitude. The accumulated air-sea heat flux of 2005, 2010, and 2013 is negative. The wintertime surface forcing resulting in the strong EDW formation is associated with NAO−. Additionally, the preconditioning is an important aiding factor to the strong 2010 EDW early spring formation and a modest aiding factor for 2005 and 2013.

The year 2012 is an extreme year of weak EDW formation (marked in "•" in Table 3). The contributing factors include the Ekman heat convergence and the positive air-sea surface heat flux. The Ekman score is 1.8, where the positive sign indicates convergence. The air-sea surface heat flux is 1.9. Its positive sign indicates weaker than average air-sea surface heat loss. The contribution from the preconditioning is relatively weak compared to the Ekman and the air-sea heat fluxes. Its score is 0.9. Its positive sign indicates an unfavorable preconditioning. The total score is 4.3 due to weak atmospheric forcings putting into perspective the EDW ventilated volume has a score of −0.9 for this year of weaker than average EDW formation.

Among the extreme years of weak EDW formation, in 2008 and 2012, both the accumulated Ekman heat flux and the accumulated air-sea surface heat flux are positive with large amplitudes (Table 3). The wintertime surface forcing resulting in the weak EDW formation is associated with NAO+. In comparison, the preconditionings of these 2 years have less important impact on their EDW formations.

Lastly, the 2014–2017, four consecutive years experienced weak EDW formation, led by 2014, an extreme year of weak EDW formation. The contributing factors of 2014 include the positive Ekman heat flux, with a score of 2.7, the positive accumulated air-sea surface heat flux, with a score of 1.8, and the unfavorable preconditioning with a score of 1.1 (Table 3). All listed factors contribute to this weak EDW formation of 2014. As the years progress, the preconditioning stays unfavorable to deep convection, so that in 2016 and 2017, the Ekman heat convergence did not have to be strong, in order to result in weak EDW formations. The weak EDW formation is driven by a sustained strong stratification in the early spring, anomalously unfavorable to the EDW formation. Yet, this anomalous unfavorable preconditioning is eroded slowly, notably within the 3 consecutive years of 2017–2019 when the EDW volume anomaly switched to positive (Table 3).

4. Conclusions

We investigated the EDW bulk that is renewed through surface ventilation in the early spring of each year. We employed four gridded observational data products, namely, ISAS, EN4, Scripps, and IPRC to calculate the EDW volume. Based on the mean interannual time series of the EDW volume, we determined the winters of 2004–2005, 2009–2010, and 2012–2013 to be extreme years of strong EDW formation. We determined the winters of 2007–2008, 2008–2009, 2011–2012, and 2013–2014 as the extreme years of weak EDW formation.

This study focuses on the interannual time scales and we found that on these interannual time scales the Ekman heat flux was the leading driver to the extreme EDW formation. The role of the Ekman heat flux varies depending on the considered time scales. Looking to the time-mean picture Maze et al. (2013) showed that the air-sea surface buoyancy loss near the Gulf Stream (the diabatic PV flux) is the dominant factor of potential vorticity sink, the contribution of the Ekman term being one order of magnitude smaller. The decreasing EDW volume on the decadal trend since 2010 reported by Stevens et al. (2020) was ascribed to surface ocean warming and AMOC weakening. In 2009, which was identified, as an extreme year of weak EDW formation, Billheimer and Talley (2013) showed an average 2009 wintertime forcing, including an average wintertime air-sea surface heat loss, suggesting an average EDW renewal. Our study reveals that the weak EDW formation in 2009 results rather from the extreme strong Ekman heat convergence.

During the strong EDW formation years, the western subtropical North Atlantic region experienced wintertime low surface level pressure on average, as part of the NAO− (Table 3). During the wintertime (September-March) of strong extreme EDW formation, strong wintertime NAO− is sufficiently represented by several strong passing storms, most notably, remnants of hurricanes and US east coast snowstorms. These strong storms are heralded by strong air-sea surface heat loss as well as large Ekman heat divergence. Particularly, this large Ekman heat divergence is a good indicator to the extreme years of strong EDW formation.

During the weak EDW formation years, the western subtropical North Atlantic region experienced wintertime high surface level pressure on average, as part of the NAO+ (Table 3). Under the high anomalous surface level pressure, we observed less strong storms passing by the EDW formation region. Correspondingly, we observed weak air-sea surface heat loss as well as Ekman heat convergence. Particularly, this Ekman heat convergence is a good indicator to the extreme years of weak EDW formation.

The preconditioning plays the auxiliary role to the EDW formation. Of all the strong EDW formation years, the preconditioning does not play as dominant a role as the Ekman heat advection. However, unfavorable

preconditioning can often serve as an aiding factor, combined with weak air-sea surface loss, to a weak EDW formation, for example, 2014–2015, 2015–2016, and 2016–2017. Under the unfavorable preconditioning of these two periods, a more buoyant and stratified water column in the late fall, hindered the wintertime EDW ventilation to the surface. Unfavorable preconditionings of 2014–2015, 2015–2016, and 2016–2017, well correspond with the weak EDW formations from previous years, 2013–2014, 2014–2015, and 2015–2016, respectively.

Data Availability Statements

The data used for the conclusion of this paper are archived in data repositories. The ocean temperature and salinity are taken from the following gridded observational datasets: EN4 (at https://www.metoffice.gov.uk/hadobs/en4/download-en4-2-1.html), ISAS (at https://www.seanoe.org/data/00412/52367/),Scripps (at http://sio-argo.ucsd.edu/RG_Climatology.html), and IPRC (at http://apdrc.soest.hawaii.edu/projects/Argo/data/gridded/On_standard_levels/index-1.html). The sea surface height are derived from the SSH anomaly (at https://resources.marine.copernicus.eu/) and MDT (at https://www.aviso.altimetry.fr/en/data/products/auxiliary-products/mdt/mdt-description.html). On the atmospheric side, the sea level pressure, the air-sea surface fluxes, the surface wind speed, and the surface wind stress momentum flux are taken from NCEP and ERA. Both NCEP and ERA are accessible online and can be found following the following links: NCEP at https://psl.noaa.gov/data/gridded/data.ncep.reanalysis.html and ERA at https://www.ecmwf.int/en/forecasts/datasets/reanalysis-datasets/era-interim.

References

APDRC. (2009). *International pacific research center. Asia-Pacific Data-Research Center*. Retrieved from http://apdrc.soest.hawaii.edu/projects/Argo/data/Documentation/gridded-var.pdf

Betts, N., Orford, J., White, D., & Graham, C. (2004). Storminess and surges in the south-western approaches of the eastern North Atlantic: The synoptic climatology of recent extreme coastal storms. *Marine Geology*, *210*(1–4), 227–246. https://doi.org/10.1016/j.margeo.2004.05.010

Billheimer, S., & Talley, L. (2016). Extraordinarily weak eighteen degree water production concurs with strongly positive north atlantic oscillation in late winter 2014/15 [in "state of the climate in 2015"]. *Bulletin of the American Meteorological Society*, *97*(8), S78–S79.

Billheimer, S., & Talley, L. D. (2013). Near cessation of eighteen degree water renewal in the western north atlantic in the warm winter of 2011–2012. *Journal of Geophysical Research: Oceans*, *118*(12), 6838–6853. https://doi.org/10.1002/2013jc009024

Blake, E. S., Kimberlain, T. B., Berg, R. J., Cangialosi, J. P., & Beven Ii, J. L. (2013). Tropical cyclone report: Hurricane sandy. *National Hurricane Center*, *12*, 1–10

Cassou, C., Terray, L., Hurrell, J. W., & Deser, C. (2004). North atlantic winter climate regimes: Spatial asymmetry, stationarity with time, and oceanic forcing. *Journal of Climate*, *17*(5), 1055–1068. https://doi.org/10.1175/1520-0442(2004)017<1055:nawcrs>2.0.co;2

CMEMS. (2020). *Global ocean gridded l4 sea surface heights and derived variables reprocessed (1993-ongoing)*. E.U. Copernicus Marine Service Information. Retrieved from https://resources.marine.copernicus.eu/?option=com_csw&view=details&product_id=SEALEVEL_GLO_PHY_L4_REP_OBSERVATIONS_008_047

de Boyer Montégut, C., Madec, G., Fischer, A. S., Lazar, A., & Iudicone, D. (2004). Mixed layer depth over the global ocean: An examination of profile data and a profile-based climatology. *Journal of Geophysical Research: Oceans*, *109*(C12), C12003. https://doi.org/10.1029/2004JC002378

Dee, D. P., Uppala, S. M., Simmons, A., Berrisford, P., Poli, P., Kobayashi, S., et al. (2011). The era-interim reanalysis: Configuration and performance of the data assimilation system. *Quarterly Journal of the Royal Meteorological Society*, *137*(656), 553–597. https://doi.org/10.1002/qj.828

Dong, S., & Kelly, K. A. (2004). Heat budget in the gulf stream region: The importance of heat storage and advection. *Journal of Physical Oceanography*, *34*(5), 1214–1231. https://doi.org/10.1175/1520-0485(2004)034<1214:hbitgs>2.0.co;2

Feucher, C., Maze, G., & Mercier, H. (2019). Subtropical mode waters and permanent pycnocline properties in the world ocean. *Journal of Geophysical Research: Oceans*, *124*(2). 10.1029/2018JC014526

Forget, G., Maze, G., Buckley, M., & Marshall, J. (2011). Estimated seasonal cycle of north atlantic eighteen degree water volume. *Journal of Physical Oceanography*, *41*(2), 269–286. https://doi.org/10.1175/2010jpo4257.1

Good, S. A., Martin, M. J., & Rayner, N. A. (2013). En4: Quality controlled ocean temperature and salinity profiles and monthly objective analyses with uncertainty estimates. *Journal of Geophysical Research: Oceans*, *118*(12), 6704–6716. https://doi.org/10.1002/2013jc009067

Haak, U., & Ulbrich, U. (1996). Verification of an objective cyclone climatology for the north atlantic. *Meteorologische Zeitschrift*, *5*, 24–30. https://doi.org/10.1127/metz/5/1996/24

Kalnay, E., Kanamitsu, M., Kistler, R., Collins, W., Deaven, D., Gandin, L., et al. (1996). The ncep/ncar 40-year reanalysis project. *Bulletin of the American Meteorological Society*, *77*(3), 437–471. https://doi.org/10.1175/1520-0477(1996)077<0437:tnyrp>2.0.co;2

Kolodziejczyk, N., Prigent-Mazella, A., & Gaillard, F. (2017). Isas-15 temperature and salinity gridded fields. *SEANOE*, *10*, 52367. https://doi.org/10.17882/52367

Li, K. (2020). *Ekman transport: A trigger of interannual extreme formation rates of eighteen degree water (theses, Université de Bretagne occidentale - Brest)*. Retrieved from https://tel.archives-ouvertes.fr/tel-03348108

Liberato, M. L. (2014). The 19 january 2013 windstorm over the North atlantic: Large-scale dynamics and impacts on iberia. *Weather and Climate Extremes*, *5*, 16–28. https://doi.org/10.1016/j.wace.2014.06.002

Marshall, J. C., Williams, R. G., & Nurser, A. G. (1993). Inferring the subduction rate and period over the north atlantic. *Journal of Physical Oceanography*, *23*(7), 1315–1329. https://doi.org/10.1175/1520-0485(1993)023<1315:itsrap>2.0.co;2

Maze, G., Deshayes, J., Marshall, J., Tréguier, A.-M., Chronis, A., & Vollmer, L. (2013). Surface vertical pv fluxes and subtropical mode water formation in an eddy-resolving numerical simulation. *Deep Sea Research Part II: Topical Studies in Oceanography*, *91*, 128–138. https://doi.org/10.1016/j.dsr2.2013.02.026

Maze, G., Forget, G., Buckley, M., Marshall, J., & Cerovecki, I. (2009). Using transformation and formation maps to study the role of air–sea heat fluxes in north atlantic eighteen degree water formation. *Journal of Physical Oceanography*, *39*(8), 1818–1835. https://doi.org/10.1175/2009jpo3985.1

NWS. (2015). *December 19-20, 2012 blizzard*. National Weather Service. Retrieved from https://www.weather.gov/dmx/dec20blizzard

NWS. (2016). *December 20, 2012 blizzard*. National Weather Service. Retrieved from https://www.weather.gov/dvn/Blizzard2012Recap

NWS. (2019). *February 25, 2013 blizzard*. National Weather Service. Retrieved from https://www.weather.gov/ama/feb25blizzard

Peng, G., Chassignet, E. P., Kwon, Y.-O., & Riser, S. C. (2006). Investigation of variability of the north atlantic subtropical mode water using profiling float data and numerical model output. *Ocean Modelling*, *13*(1), 65–85. https://doi.org/10.1016/j.ocemod.2005.07.001

Piron, A., Thierry, V., Mercier, H., & Caniaux, G. (2017). Gyre-scale deep convection in the subpolar north atlantic ocean during winter 2014–2015. *Geophysical Research Letters*, *44*(3), 1439–1447. https://doi.org/10.1002/2016gl071895

Qiu, B., & Huang, R. X. (1995). Ventilation of the North atlantic and north pacific: Subduction versus obduction. *Journal of Physical Oceanography*, *25*(10), 2374–2390. https://doi.org/10.1175/1520-0485(1995)025<2374:votnaa>2.0.co;2

Rio, M. (2009). A new mean dynamic topography computed over the global ocean from grace data, altimetry and in situ measurements. In *Poster communication at oceanobs09 symposium* (pp. 21–25).

Roemmich, D., & Gilson, J. (2009). The 2004–2008 mean and annual cycle of temperature, salinity, and steric height in the global ocean from the argo program. *Progress in Oceanography*, *82*(2), 81–100. https://doi.org/10.1016/j.pocean.2009.03.004

Ryan, M. S., Gerhardt, M. B., Hamrick, D., Kocin, P. J., Kong, K.-Y., Otto, R., & Rubin-Oster, B. (2014). *Major winter weather events during the 2012-2013 cold season*. NOAA Weather Prediction Center. Retrieved from https://www.wpc.ncep.noaa.gov/storm_summaries/event_reviews/2012-2013ColdSeasonArticle.pdf

Stevens, S. W., Johnson, R. J., Maze, G., & Bates, N. R. (2020). A recent decline in north atlantic subtropical mode water formation. *Nature Climate Change*, *10*(4), 335–341. https://doi.org/10.1038/s41558-020-0722-3

Thomas, L. N. (2005). Destruction of potential vorticity by winds. *Journal of Physical Oceanography*, *35*(12), 2457–2466. https://doi.org/10.1175/jpo2830.1

Thomas, L. N., Taylor, J. R., Ferrari, R., & Joyce, T. M. (2013). Symmetric instability in the gulf stream. *Deep Sea Research Part II: Topical Studies in Oceanography*, *91*, 96–110. https://doi.org/10.1016/j.dsr2.2013.02.025

Vincent, E. M., Lengaigne, M., Madec, G., Vialard, J., Samson, G., Jourdain, N. C., & Jullien, S. (2012). Processes setting the characteristics of sea surface cooling induced by tropical cyclones. *Journal of Geophysical Research: Oceans*, *117*(C2). https://doi.org/10.1029/2011jc007396

Vincent, E. M., Madec, G., Lengaigne, M., Vialard, J., & Koch-Larrouy, A. (2013). Influence of tropical cyclones on sea surface temperature seasonal cycle and ocean heat transport. *Climate Dynamics*, *41*(7–8). https://doi.org/10.1007/s00382-012-1556-0

Williams, R. (2001). Ocean subduction. *Management*, *25*(1). https://doi.org/10.1006/rwos.2001.0109

Williams, R. G., Marshall, J. C., & Spall, M. A. (1995). Does stommel's mixed layer "demon" work? *Journal of Physical Oceanography*, *25*(12), 3089–3102. https://doi.org/10.1175/1520-0485(1995)025<3089:dsmlw>2.0.co;2

Zunino, P., Mercier, H., & Thierry, V. (2020). Why did deep convection persist over four consecutive winters (2015–2018) southeast of cape farewell? *Ocean Science*, *16*(1), 99–113. https://doi.org/10.5194/os-16-99-2020